Combust. Sci. and Tech., 180: 1–26, 2008

ISSN: 0010-2202 print/1563-521X online
DOI: 10.1080/00102200701486873

Taylor & Francis
Taylor & Francis Group

VAPORIZATION OF LIQUID OXYGEN (LOX) DROPLETS IN HYDROGEN AND WATER ENVIRONMENTS UNDER SUB- AND SUPER-CRITICAL CONDITIONS

Patrick Lafon[1], Hua Meng[1], Vigor Yang[1,*], and Mohammed Habiballah[2]

[1]*Department of Mechanical and Nuclear Engineering, The Pennsylvania State University, University Park, PA*

[2]*Office National d'Etudes et de Recherche Aérospatiale, Châtillon, France*

This article presents a comprehensive numerical analysis of liquid oxygen (LOX) droplet vaporization in quiescent hydrogen and water environments over a broad range of ambient conditions. The theoretical formulation is based on a complete set of conservation equations of mass, momentum, energy, and species concentrations in a spherically symmetric coordinate. A self-consistent and efficient method for evaluating transport properties and a unified treatment of general fluid thermodynamics are incorporated into an implicit finite-volume numerical scheme. The analysis is further equipped with a water-vapor condensation model for treating the phase change near the droplet surface. The effects of the Dufour and Soret cross-diffusion terms are explored and found to exert negligible influences on the droplet lifetime. Various issues associated with high-pressure droplet vaporization are investigated. In addition, correlations for droplet lifetimes are established for both LOX/hydrogen/water systems in terms of the initial droplet diameter, reduced critical temperature of oxygen, and thermal conductivities of oxygen and ambient gases.

Keywords: Irreversible thermodynamic theorem; Subcritical and supercritical droplet vaporization; Water vapor condensation

INTRODUCTION

In many liquid-fueled combustion devices, the chamber pressures and temperatures may well exceed the thermodynamic critical conditions of injected fuels. Examples include diesel, gas-turbine, and liquid-propellant rocket engines. Liquid fuel is usually injected into the chamber at a subcritical temperature, and breaks up into small droplets through atomization, which then undergo a sequence of vaporization, mixing, and burning processes. The droplet vaporization rate under supercritical conditions has significant impact on combustor performance and has attracted enormous research interest (Sirignano and Delplanque, 1999; Bellan, 2000; Yang, 2001).

Received 6 January 2006; accepted 23 May 2007.

Current address for Prof. Hua Meng, Center for Engineering and Scientific Computation and College of Computer Science, Zhejiang University, Hangzhou, Zhejiang 310027, P.R. China. E-mail: menghua@zju.edu.cn

*Address correspondence to vigor@psu.edu

The majority of existing studies have focused on the vaporization and combustion of isolated droplets in quiescent environments. Both hydrocarbon droplets evaporating and burning in air (Hsieh et al., 1991; Shuen et al., 1992; Curtis and Farrel, 1992; Jia and Gogos, 1993) and liquid oxygen (LOX) droplets in hydrogen environments (Litchford and Jeng, 1990; Delplanque and Sirignano, 1993; Yang et al., 1994; Daou et al., 1995; Harstad and Bellan, 1998a) have been treated comprehensively. Emphasis was placed on the effects of transient diffusion, property variations, interfacial thermodynamics, and dissolution of ambient gases into the liquid droplet. In addition, droplet interactions and associated transport phenomena have been investigated (Jiang and Chiang, 1994, 1996; Harstad and Bellan, 1998b; Meng and Yang, 1998).

Droplet vaporization in convective environments presents serious challenges both physically and numerically. Effects of free-stream velocity on droplet lifetime and dynamics have only been addressed recently by Daou and Rogg (1998) and Meng et al. (2005). The latter study considered LOX droplet vaporization in supercritical hydrogen streams over a broad range of pressures and Reynolds numbers. The formulation was based on a unified treatment of general fluid thermodynamics and a robust preconditioning numerical scheme (Meng and Yang, 2003). Various fundamental issues associated with droplet dynamics and related transport phenomena at high pressures were examined systematically, with special attention given to the distinct characteristics of cryogenic fluids. Correlations of the mass and momentum transfer between droplet and free stream were established in terms of droplet thermodynamic state and ambient flow conditions. The results can be effectively used as a physical submodel for high-pressure spray combustion analyses.

In rocket engines using oxygen and hydrogen as propellants, the combustion products contain a substantial amount of water vapor. Since water is less volatile and its critical pressure and temperature are much higher than those of oxygen and hydrogen (see Table 1), the issue of water-vapor condensation in the low temperature region near the droplet surface must be considered. Powell (1988) experimentally investigated the water-vapor condensation on LOX droplet surface by using liquid nitrogen droplets as a simulant in superheated steam at the atmospheric pressure. The same phenomenon was examined in the numerical study of Litchford and Jeng (1990). No comprehensive research, however, has been conducted at high pressures.

In this article, a comprehensive numerical analysis of LOX droplets evaporating in hydrogen and water environments is conducted under both sub- and super-critical conditions. The theoretical formulation is based on a complete set of conservation equations of mass, momentum, energy, and species concentrations. A self-consistent and efficient method for evaluating transport properties (Meng et al., 2005) and a unified treatment of general fluid thermodynamics (Meng and

Table 1 Critical properties of oxygen, hydrogen, and water

	Oxygen	Hydrogen	Water
p_c (atm)	49.8	12.8	218.3
T_c (K)	154.6	33.1	647.3

Yang, 2003) are incorporated into an implicit finite-volume numerical scheme. The analysis is further equipped with a water-vapor condensation model for treating the phase change near the droplet surface. In addition, the effects of the Dufour and Soret cross-diffusion terms are explored. Results for droplet lifetimes are correlated in terms of the initial droplet properties and ambient conditions for both LOX/hydrogen and LOX/hydrogen/water systems.

THEORETICAL FORMULATION AND NUMERICAL SOLUTION

In the present study, forced convection and buoyancy effects are neglected. The problem is thus governed by a set of conservation equations in a spherically symmetric coordinate system.

Conservation Equations

For an arbitrary control volume $V(t)$ and its control surface $A(t)$, which moves at a speed $\vec{w}$ in a stationary reference frame, the conservation equations can be written in the following forms:
Mass conservation

$$\frac{d}{dt}\int_{V(t)} \rho dV + \int_{A(t)} \rho(\vec{v}-\vec{w})\cdot\vec{n}dA = 0 \tag{1}$$

Momentum conservation

$$\nabla p = 0 \tag{2}$$

Energy conservation

$$\frac{d}{dt}\int_{V(t)} \rho e_t dV + \int_{A(t)} \rho(\vec{v}-\vec{w})e_t\cdot\vec{n}dA = -\int_{A(t)} \vec{q}_e\cdot\vec{n}dA - \int_{A(t)} p\vec{v}\cdot\vec{n}dA \tag{3}$$

Species conservation

$$\frac{d}{dt}\int_{V(t)} \rho Y_i dV + \int_{A(t)} \rho Y_i(\vec{v}-\vec{w})\cdot\vec{n}dA = -\int_{A(t)} \vec{q}_i\cdot\vec{n}dA + \int_{V(t)} \dot{\omega}_i dV \tag{4}$$

where the subscript i ranges from 1 to $N-1$, and the parameter N represents the total number of species. Standard notations in fluid mechanics are used here, with ρ, p, $\vec{v}$, e_t, and Y_i being the density, pressure, velocity vector, specific total energy, and mass fraction of species i, respectively. The source term $\dot{\omega}_i$ in Eq. (4) arises from mass production/destruction in chemical reactions.

The momentum equation, Eq. (2), is simplified based on an assumption that the velocities involved in the vaporization process are very low, a condition valid in the present study. The energy-diffusion term contains contributions from heat conduction, mass diffusion, and thermal diffusion (i.e., the Dufour effect), while the mass-diffusion term consists of contributions from both concentration (i.e.,

Fick's law) and temperature (i.e., the Soret effect) gradients. The Soret and Dufour effects may be significant because of the disparity of the molecular weights between hydrogen and oxygen and the steep temperature gradient involved. The overall diffusion fluxes take the following forms:

$$\vec{q}_e = -\lambda \nabla T - \sum_i^N \vec{q}_i \bar{h}_i + R_u T \sum_i^N \sum_j^N \frac{X_j D_{Ti}}{W_i D_{ij}} (V_i - V_j) \tag{5}$$

$$\vec{q}_i = \rho Y_i V_i = -\rho D_{im} \nabla Y_i - D_{Ti} \frac{\nabla T}{T} \tag{6}$$

For more details regarding the theoretical formulation, refer to Meng et al. (2005).

Interfacial Boundary Conditions

Until the droplet surface reaches its critical mixing state, thermodynamic phase equilibrium prevails at this location, and can be expressed as

$$T^g = T^l,\ p^g = p^l,\ \mu_i^g = \mu_i^l \tag{7}$$

where μ_i^l and μ_i^g represent chemical potentials in the liquid and gas phases, respectively. In addition, mass, energy, and species are conserved across the droplet surface.

$$\dot{m} = \rho(\vec{v} - \dot{\vec{R}}) \cdot \vec{n} A\big|_{r=R_+} = \rho(\vec{v} - \dot{\vec{R}}) \cdot \vec{n} A\big|_{r=R_-} \tag{8a}$$

$$\dot{m}_i = [\dot{m} Y_i + \vec{q}_i \cdot \vec{n} A]_{r=R_+} = [\dot{m} Y_i + \vec{q}_i \cdot \vec{n} A]_{r=R_-} \tag{8b}$$

$$-\lambda \nabla T|_{r=R_-} = -\lambda \nabla T|_{r=R_+} + \sum_{i=1}^N \dot{m}_i (\bar{h}_i^g - \bar{h}_i^l) \tag{8c}$$

where $\dot{R}$ is the droplet regression rate, $\dot{m}$ the mass vaporization rate, and $\dot{m}_i$ the vaporization rate of species i. The unit vector $\vec{n}$ normal to the droplet surface is positive pointing outwards.

Droplet Vaporization Rate

A robust and efficient treatment is developed to handle thermodynamic equilibrium conditions and the conservation of mass, energy, and species concentrations. The formulation is based on Onsager's irreversible thermodynamics theorem (Callen, 1985), which states that temperature difference is the driving force for heat transfer, pressure difference for fluid flow, and chemical potential difference for species transfer. Species vaporization rates across the droplet interface are, therefore,

proportional to the chemical potential differences between the liquid and gas phases. The theorem is applicable to any purely resistive system in the following form:

$$\dot{m}_i = K_{vap,i}(\mu_i^l - \mu_i^g) \tag{9}$$

In deriving this expression, the system is allowed to deviate slightly from thermodynamic equilibrium. Therefore, high-order terms can be neglected, resulting in a linear phenomenological relationship similar to Fourier's law for heat conduction and Fick's law for species diffusion. The assumption also implies that Eq. (7) is not exactly satisfied, but the non-equilibrium state is close to the equilibrium one when a large vaporization kinetic coefficient $K_{vap,i}$ (for example, 100) is used. Numerical results indicate that the final solution is not sensitive to this parameter; an order-of-magnitude change of $K_{vap,i}$ produces negligible variations in the final calculations. This technique is especially compatible with our implicit numerical scheme, providing an efficient and accurate solution procedure. The same technique is also applicable to the energy transfer across the droplet surface. Since pressure equilibrium has already been established by the isobaric condition, Eq. (2), throughout the entire field, thermodynamic phase equilibrium is thus closely approached at the droplet surface. As soon as the droplet surface reaches the critical mixing state, the above numerical procedure is replaced by a single-phase supercritical-fluid treatment.

Liquid Water Condensation

The combustion of oxygen and hydrogen produces water vapor, which is much less volatile than oxygen and hydrogen. Once a substantial amount of water vapor reaches the low-temperature region near the droplet surface, its partial pressure becomes higher than the corresponding saturation value, leading to condensation and formation of liquid water particles. The ensuing influence on the local temperature field and LOX droplet behavior may not be neglected.

The water-condensation mechanism involves an array of complex processes, including nucleation and particle growth through germination. In addition, particles may interact with the gaseous flow and with each other. Particle formation is attributed to nucleation of molecular clusters called embryos. As the saturation ratio, defined as the ratio of the partial pressure of the water vapor to its saturation value ($S = p_{H_2O}/p_{sat}$), increases above unity, embryos larger than a critical size become stable water particles (Reist, 1984). This critical size R_{pc} can be estimated from the Kelvin equation given by McDonald (1962)

$$R_{pc} = \frac{2\sigma}{R_u \rho_p T \ln S} \tag{10}$$

where σ is the surface tension of water, and ρ_p its density. These two parameters are approximately equal to 7.5×10^{-2} N/m and 1000 kg/m^3, respectively. The expression is valid only for a saturation ratio greater than unity. If the ratio is less than unity, embryos disintegrate as rapidly as they form. Figure 1 presents results

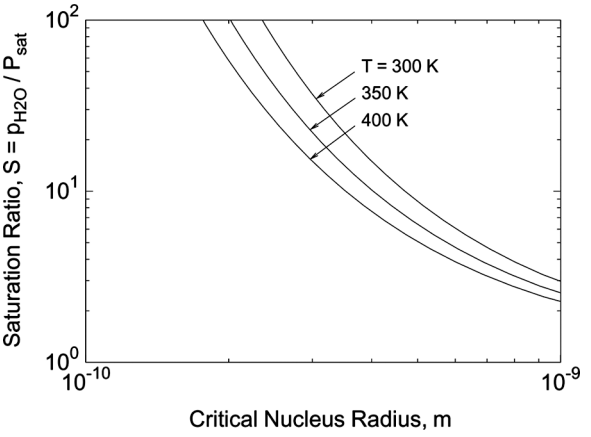

Figure 1 Variations of critical nucleus radius with saturation ratio at different temperatures.

from Eq. (10) at different temperatures. Assuming the nucleation process is not influenced by foreign molecules (oxygen and hydrogen) and is thus homogeneous, the nucleation rate per unit volume can be determined using statistical thermodynamics theories (Rogers and Yau, 1989)

$$J = 4\pi R_{pc}^2 Z \frac{p_{H_2O}}{\sqrt{2\pi W R_u T}} \frac{\rho_{H_2O} N^2}{W} \exp\left(-\frac{4\pi R_{pc}^2 \sigma N}{3 R_u T}\right) \tag{11}$$

where the factor Z denotes the Zeldovich factor, which is on the order of 10^4 when all quantities are measured in SI units, and N is the Avogadro number. Combining Eqs. (10) and (11), the nucleation rate can be expressed as a function of the saturation ratio and temperature.

For a given gaseous water density ρ_{H_2O}, the characteristic time of nucleation $\tau_{nucleation}$ can be defined as

$$\tau_{nucleation} = \frac{3\rho_{H_2O}}{4\pi R_{pc}^3 \rho_p J} \tag{12}$$

From the two previous relations, this characteristic nucleation time can also be expressed as a function of temperature and the saturation ratio. Figure 2 presents the result. This characteristic time is extremely sensitive to the saturation ratio. For example, once the saturation ratio exceeds 10 at 300 K, the nucleation time becomes less than 10^{-10} s, indicating that the nucleation process can be considered as instantaneous with respect to the vaporization process, which has a characteristic time on the order of 10^{-3} s. At such a saturation ratio, the critical radius of the nucleus is between 10^{-10} and 10^{-9} m, and contains only a limited number of water molecules.

The water saturation pressure is a function of temperature. Expressions derived from experimental data are available in the literature (Reid et al., 1987). The saturation pressure exhibits an exponential dependency on temperature, decreasing

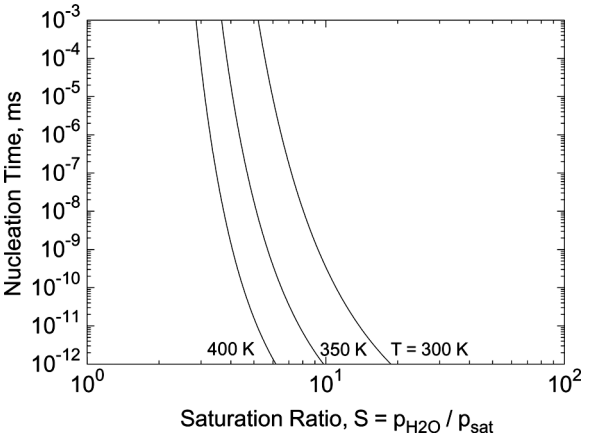

Figure 2 Variation of characteristic nucleation time with saturation ratio at different temperatures.

rapidly as temperature decreases. Water condensation thus occurs in regions with large temperature gradients. Furthermore, with the assumption of homogeneous condensation, the characteristic nucleation times are overestimated for saturation ratios close to unity.

In addition, the hydrogen and oxygen molecules are expected to influence the nucleation process as well. Based on these considerations, it is reasonable to consider that the nucleation process occurs instantaneously once the saturation ratio is slightly above unity. This hypothesis is equivalent to considering a local thermodynamic equilibrium. Calculations have been carried out with the nucleation process occurring at a range of saturation ratios up to 10. The results show negligible differences.

After their formation, condensed water particles interact with the surrounding gaseous flow and are subjected to thermophoretic and viscous forces. The former tends to attract heavier molecules or small particles to low temperature regions, as was discussed by Talbot et al. (1980). An expression for estimating the thermophoretic force is proposed by Brock (1962). In a spherically symmetric coordinate, it has the following form:

$$F_T = -\frac{12\pi\mu^2 R_p C_s(\Lambda + C_t Kn)}{\rho(1+3C_m Kn)(1+2\Lambda+2C_t Kn)}\frac{1}{T}\frac{\partial T}{\partial r} \tag{13}$$

where parameters without subscripts refer to the gaseous properties. The parameter Λ represents the ratio of the gaseous to the particle thermal conductivity, and the constants C_s, C_t and C_m are derived from the kinetic theory and have been assigned the values of 1.17, 2.18, and 1.14, respectively. The Knudsen number Kn is defined as the ratio of the molecular mean free path to the particle radius

$$Kn = \frac{\lambda}{R_p} = \frac{1}{R_p}\frac{2\mu}{\rho\sqrt{8R_u T/\pi}} \tag{14}$$

Equation (13) yields very good predictions. Talbot et al. (1980) have shown that it produces just 3% error even in the collisionless limit, $Kn \to \infty$ although it was originally designed for small values of the Knudsen number.

Since water nuclei are typically of the order of the molecular mean free path, viscous forces can be modeled using the Stokes-Cunningham equation

$$F_v = \frac{6\pi\mu R_p}{C_c}(v - v_p) \tag{15}$$

where v and v_p are the flow and particles velocities, respectively. The Cunningham correction coefficient C_c is defined as

$$C_c = 1 + Kn\left[1.257 + 0.4\exp\left(-\frac{1.1}{Kn}\right)\right] \tag{16}$$

It was introduced by Carlson and Haglund (1964) into the Stokes-flow expression to account for non-continuum effects coincident with water particle sizes, which is of the order of the molecular mean free path. Assuming that thermophoretic and viscous forces are the only forces acting on the particle, the equation of motion describing particle dynamics can be written as

$$\frac{4}{3}\pi R_p^3 \rho_p \frac{dv_p}{dt} = F_v + F_T \tag{17}$$

Consequently a terminal velocity of a water particle is reached when the net force acting on the particle is equal to zero. Based on Eqs. (13) and (15), this terminal velocity can be derived as

$$v_{p,terminal} = v - \frac{2C_c C_s \mu(\Lambda + C_t Kn)}{\rho(1 + 3C_m Kn)(1 + 2\Lambda + 2C_t Kn)}\frac{1}{T}\frac{\partial T}{\partial r} \tag{18}$$

Numerical analyses show that the second term on the right-hand side is much smaller than the first one. The terminal velocity is thus very close to the gaseous flow velocity.

The time needed to reach this mechanical equilibrium can be obtained as

$$\tau_{mechanical\ equilibrium} = \frac{R_p^2 \rho_p C_c}{18\mu} \tag{19}$$

Figure 3 presents the time to mechanical equilibrium as a function of particle radius and temperature. It clearly shows that this characteristic time is several orders of magnitude smaller than the droplet lifetime. We can thus assume that a particle reaches its terminal velocity instantaneously after formation.

The condensation effects can now be modeled as a sink term, $-\dot{m}_{cond}$, in the mass conservation equation, and a source term, $\dot{m}_{cond}\Delta h_{vap,H_2O}$, in the energy conservation equation. The species conservation equation of water does not need to be solved, as the conservation equations of hydrogen and oxygen are solved instead.

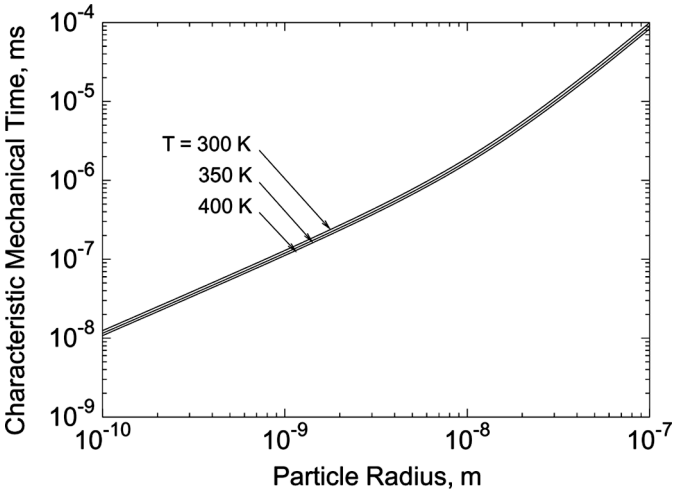

Figure 3 Characteristic time to mechanical equilibrium as a function of particle radius at different temperatures.

The mass condensation rate of the water vapor can be calculated using pressure differences based on Onsager's irreversible theorem (Callen, 1985).

$$\dot{m}_{cond} = K_{cond,H_2O}(p_{H_2O} - p_{sat}) \tag{20}$$

where the two pressures are the partial pressure of water vapor and its saturation pressure, respectively. Because the water vapor condenses instantaneously once its partial pressure is higher than the saturation value, the condensation parameter K_{cond,H_2O} can be taken as a large number, e.g., 100. This is the same numerical treatment as that applied to the droplet vaporization rate, described in the preceding section.

Evaluation of Properties

Models based on the ideal gas law cannot be used to evaluate fluid thermodynamic properties at high pressures. A self-consistent and efficient method has been developed in our previous work (Meng et al., 2005), which properly accounts for dense-fluid corrections.

Accurate evaluation of transport properties is crucial for studying supercritical fluid transport and dynamics. The extended corresponding-state (ECS) principle of Ely and Hanley (1981, 1983) is used herein to estimate the viscosity and thermal conductivity of the fluid mixture over its entire thermodynamic state. A simple scheme for predicting the binary mass diffusivity of a dense fluid by means of a corresponding-state approach suggested by Takahashi (1974) is employed in the present numerical analysis. Details can be found in Meng et al. (2005).

Numerical Treatment

The set of conservation equations, Eqs. (1)–(4), is solved using an implicit finite-volume numerical scheme in a spherically symmetric coordinate system. The

analysis also incorporates a unified treatment of general fluid thermodynamics and transport properties into the flow solver (Meng and Yang, 2003). In the present work, since the grid moves as the droplet surface regresses, each control volume in the computational domain must be calculated in a coupled manner. Before the droplet surface reaches the critical mixing state, the thermodynamic equilibrium conditions are enforced through the phenomenological relations derived from irreversible thermodynamics theories, Eq. (9).

After the critical mixing state is reached at the droplet surface, the enthalpy of vaporization and surface tension vanish, and the entire flow field, including both the LOX droplet and surrounding gases, becomes an essentially continuous medium without a well-defined liquid/gas interfacial boundary. The droplet interior, however, remains in the liquid state with a subcritical temperature distribution. The subsequent droplet evolution is diffusion-controlled with no effect of interfacial thermodynamics. A single-phase supercritical fluid model can then be employed.

RESULTS AND DISCUSSION

The theoretical model and numerical scheme described in the preceding sections have been numerically verified and experimentally validated against several test problems involving vaporization of n-heptane droplets in quiescent nitrogen environments under both sub- and super-critical conditions (Meng and Yang, 2003), fluid dynamics and transport phenomena of single LOX droplets in supercritical hydrogen streams (Meng et al., 2005), supercritical nitrogen jet dynamics (Zong et al., 2004; Zong and Yang, 2006), and supercritical combustion of LOX and methane of a shear co-axial injector (Zong and Yang, 2007). The present work concerns a LOX droplet evaporating in quiescent hydrogen and water environments under both sub- and super-critical conditions.

Before the droplet surface reaches the critical mixing state, thermodynamic equilibrium conditions prevail at this location, and the droplet is well defined. After the critical mixing state is reached at the droplet surface, no distinction between the droplet and ambient gas remains. To quantify the droplet gasification process, the interface can be conveniently defined by either the critical mixing temperature or the critical mixing composition at a given pressure. Application of one or the other definition leads to different results, mainly because of non-unity of the Lewis number.

The former definition is more suited for comparison with experimental measurements using optical techniques sensitive to temperature or density gradient (Hsiang and Faeth, 1992). For use in the spray analysis, in which droplet vaporization is treated as a mass source and an energy sink in the gas-phase conservation equations of mass and energy, respectively, the definition of the critical interface based on the mixing composition is preferred. The mixing process associated with the vaporized species can then be handled by an adequate gas-mixing model. In the following, results based on both definitions of the critical interface are presented.

Droplet Vaporization in Pure Hydrogen Environments

Calculations are carried out for LOX droplet vaporization in pure hydrogen over a broad range of initial and ambient conditions. This problem is entirely

controlled by the diffusion process, as discussed by Daou et al. (1995). A dimensional analysis shows that the initial droplet diameter is the only length scale, and that the droplet lifetime is proportional to the square of the initial droplet diameter. Thus, only droplets with an initial diameter of $D_0 = 100\,\mu m$ are considered here.

Cases with an ambient hydrogen temperature $T_\infty = 1000\,K$ are first calculated to provide a baseline data set. The initial droplet temperature T_0 is uniformly distributed at 90 K. Figure 4 shows transient variations of the droplet surface temperature at different pressures in both the sub- and super-critical regimes. Three different scenarios are observed. First, at low pressures ($p = 10\,atm$), the surface temperature rises rapidly and then reaches a constant value, a condition referred to as the pseudo-wet-bulb state (Hsieh et al., 1991).

This value is slightly lower than the boiling temperature of oxygen because of the dissolution of hydrogen into the droplet. Second, near the critical pressure of oxygen ($p = 50\,atm$), the droplet surface temperature increases continuously. The pseudo-wet-bulb state is never reached, and the vaporization process becomes transient in nature throughout the entire droplet lifetime. Third, for pressures greater than 100 atm, the droplet reaches its critical mixing state very quickly.

Figures 5–7 show respectively the distributions of the specific heat, thermal diffusivity, and Lewis number at different times for $p = 100\,atm$. The weak divergence of the 3 parameters around the critical interface and the disparities of properties between oxygen and hydrogen are clearly illustrated.

Figure 8a presents the time evolution of the reduced droplet diameter squared at various pressures. The isotherm of the critical mixing temperature is defined as the droplet surface. At low pressures, the droplet vaporization rate follows the predictions of the quasi-steady theory. At high pressures, the vaporization process becomes transient, and the slope dD^2/dt approaches the infinite at the beginning of the

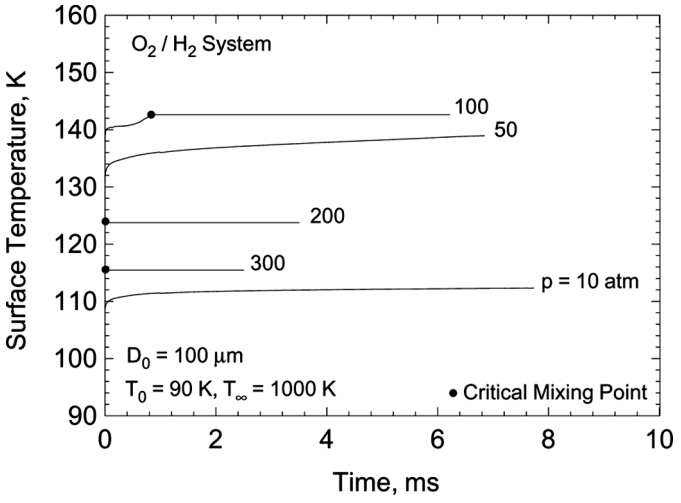

Figure 4 Transient variation of droplet surface temperature at various pressures; $T_\infty = 1000\,K$; $T_0 = 90\,K$; $D_0 = 100\,\mu m$.

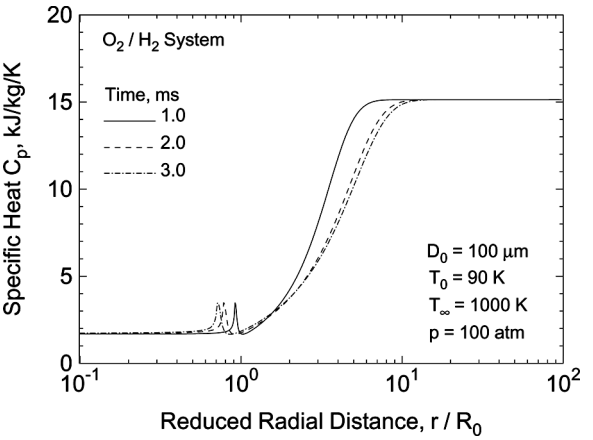

Figure 5 Distribution of specific heat over the entire field at various times; $T_0 = 90\,\mathrm{K}$, $T_{\infty.} = 1000\,\mathrm{K}$, $p = 100\,\mathrm{atm}$, $D_0 = 100\,\mu\mathrm{m}$.

process, due to the initial sharp temperature gradient at the droplet surface and the ensuing volume dilatation.

Figure 8b also presents the time evolution of the reduced droplet diameter squared at various pressures, but the droplet surface is now defined as the isopleth at the critical mixing composition. The results are substantially different from their counterparts in Figure 8a, mainly because the Lewis number is much larger than unity inside the droplet, as indicated in Figure 7. Heat transfer penetrates into the droplet interior much faster than mass diffusion, especially at higher pressures. The resultant volume dilatation pushes the critical mixing-composition line outward to a higher temperature in which mass diffusion prevails (i.e., $Le \geq 1$). This phenomenon, combined with increasing temperature in the droplet interior, explains the

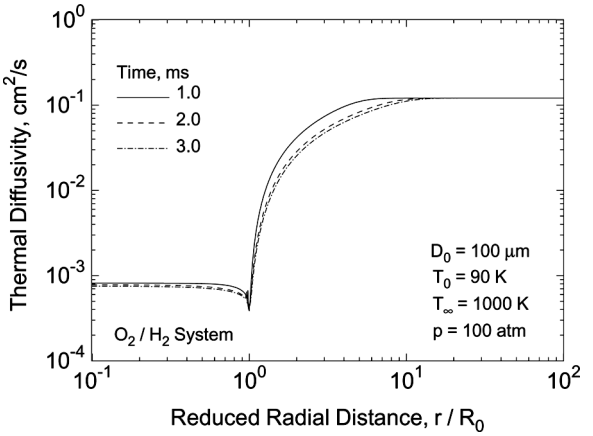

Figure 6 Distribution of thermal diffusion coefficient over the entire field at various times; $T_0 = 90\,\mathrm{K}$, $T_\infty = 1000\,\mathrm{K}$, $p = 100\,\mathrm{atm}$, $D_0 = 100\,\mu\mathrm{m}$.

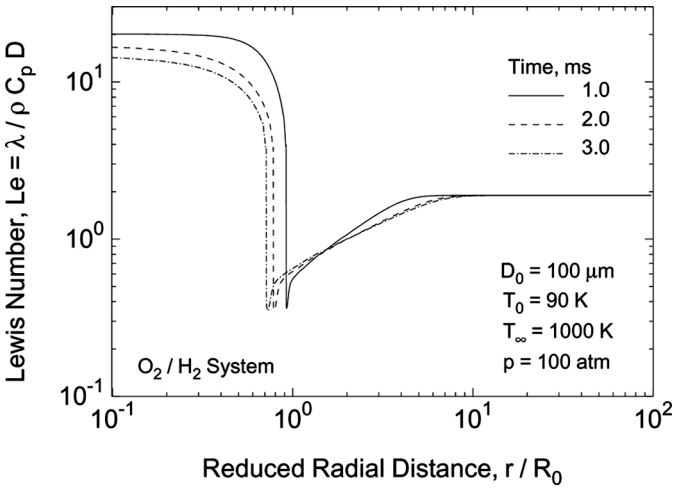

Figure 7 Distribution of Lewis number over the entire field at various times; $T_0 = 90\,\mathrm{K}$, $T_\infty = 1000\,\mathrm{K}$, $p = 100\,\mathrm{atm}$, $D_0 = 100\,\mu\mathrm{m}$.

faster droplet vaporization rate at supercritical pressures in the late stage of the vaporization process when the temperature becomes higher inside the droplet.

Figure 9a shows droplet lifetimes at various ambient temperatures and reduced pressures, defined as $p_r = p/p_{c,O_2}$. Logarithmic scales are used in this figure on both coordinate axes. At a given ambient temperature, the droplet lifetime exhibits 2 different slopes, depending on whether the vaporization process is in the subcritical or supercritical regime. In the subcritical regime, the droplet lifetime decreases with increasing pressure, largely due to the reduced enthalpy of vaporization. In the supercritical regime, the droplet behavior is dictated by thermal diffusion.

With increasing pressure, the decrease of the critical mixture temperature combined with the increase of the thermal conductivity leads to decreasing droplet lifetimes. No abrupt change is observed in the transition region despite the vanishing of the enthalpy of vaporization. As the critical mixing condition is approached, the specific heat of the mixture at the droplet surface exhibits a divergence, as shown in Figure 5. Consequently, the amount of energy needed to increase the droplet temperature becomes larger. Effects of the vanishing enthalpy of vaporization and the diverging specific heat tend to balance each other.

Figure 9b shows droplet lifetimes based on the definition of the droplet surface as the isopleth of the critical mixing composition. The droplet lifetime decreases with increasing pressure, but levels off at very high pressures. This phenomenon can be attributed to the combined effects of the temperature sensitivity of the Lewis number and the volume dilatation of the droplet interior, which tends to retard the regression of the critical mixing-composition line. At a low ambient temperature, the droplet lifetime may even increase slightly in the supercritical pressure regime. Under this circumstance, a minimum droplet lifetime occurs at an intermediate pressure above the oxygen critical pressure.

To consider the influences of the cross-diffusion (Soret and Dufour) effects, two series of calculations, with and without these effects, have been conducted.

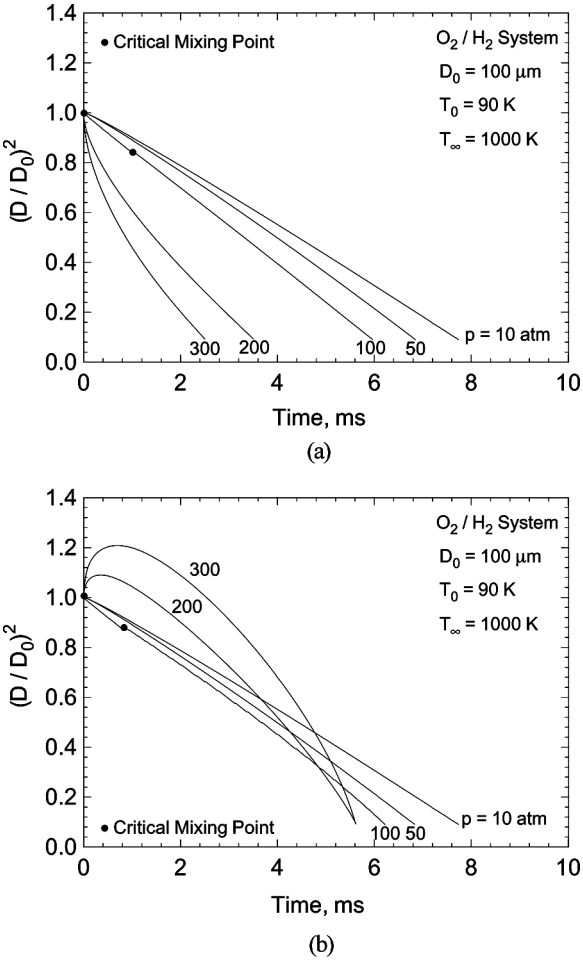

Figure 8 Transient variations of the reduced droplet diameter squared at various pressures; droplet surface defined as (a) the isotherm of the critical mixing temperature and (b) the isopleth of the critical mixing composition; $T_0 = 90\,\mathrm{K}$, $T_\infty = 1000\,\mathrm{K}$, $D_0 = 100\,\mu\mathrm{m}$.

Results are reported in Figures 10a and 10b with different definitions of the droplet surface. The effects of the cross-diffusion terms are observed for both cases, especially in Figure 10b, in which the droplet surface is defined as the isopleth of the critical mixing composition. The Soret effects tend to attract heavier molecules into low temperature zones and lighter molecules into high temperature zones.

As a consequence, oxygen moves toward the droplet surface while hydrogen in the opposite direction, thereby increasing the droplet lifetime. In the present study, the estimation of the cross-diffusion coefficients neglects the pressure effects. In reality, the dependency of these coefficients with respect to pressure is roughly the same as the mass diffusion coefficient, which decreases with increasing pressure. Therefore, the effects of the cross-diffusion terms have been over-estimated in the

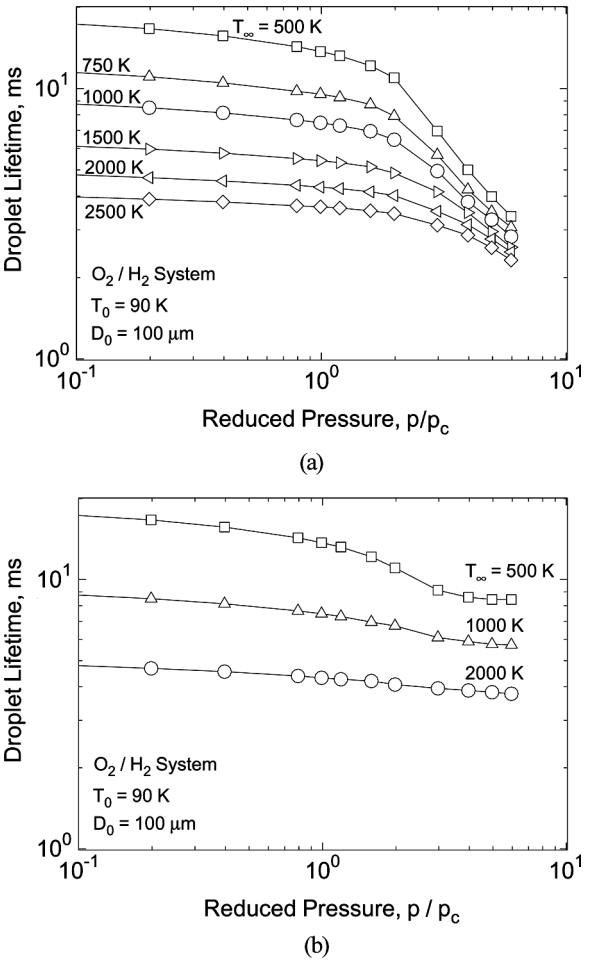

Figure 9 Droplet lifetime as a function of reduced pressure at various ambient temperatures; droplet surface defined as (a) the isotherm of the critical mixing temperature and (b) the isopleth of the critical mixing composition; $T_0 = 90\,\mathrm{K}$, $D_0 = 100\,\mu\mathrm{m}$.

present study. Based on the comparisons, the cross-diffusion terms exert negligible influence in determining the droplet lifetime.

Figure 11 shows the limiting ambient temperatures at which the critical mixing condition can be reached for various pressures and two different initial droplet temperatures, 90 and 110 K. The dashed lines correspond to the critical mixing condition reached after 1% of the droplet mass is evaporated, and the solid lines correspond to the critical mixing condition reached at the end of the droplet vaporization process. For ambient pressures and temperatures located in the region above the dashed line, the supercritical regime can be reached almost instantaneously once the droplet is placed in the environment. With increasing ambient pressure, the supercritical regime can be reached at a lower ambient temperature, because of the decreased enthalpy of vaporization and critical mixing temperature of the droplet with increasing pressure.

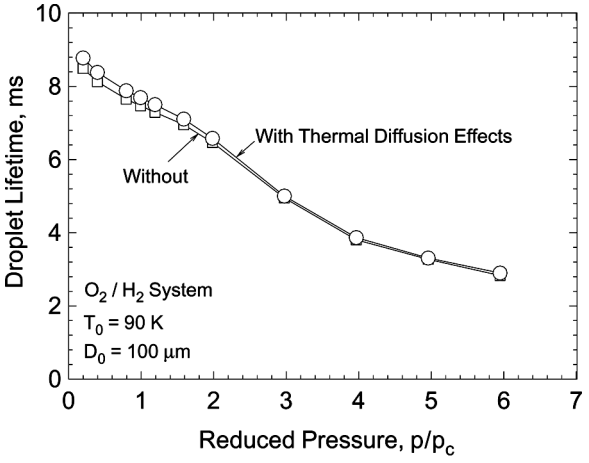

(a)

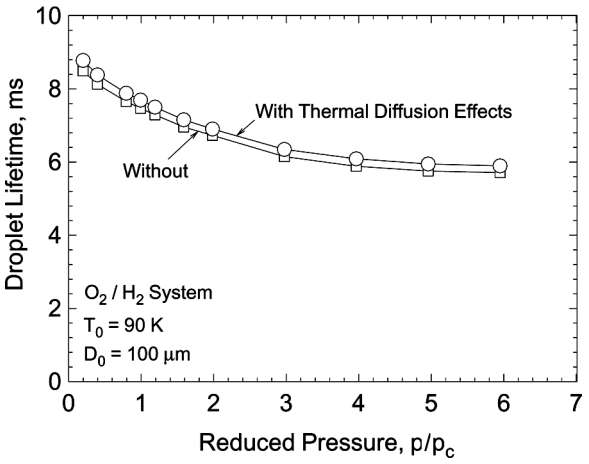

(b)

Figure 10 Effects of cross-diffusion terms on droplet lifetime at various pressures; droplet surface defined as (a) the isotherm of the critical mixing temperature and (b) the isopleth of the critical mixing composition; $T_\infty = 1000\,\mathrm{K}$; $T_0 = 90\,\mathrm{K}$; $D_0 = 100\,\mu\mathrm{m}$.

In addition, with increasing initial droplet temperature, the supercritical regime becomes easier to reach.

An important goal for the present study is to establish a correlation for estimating the droplet lifetime under a broad range of conditions. The result can also be used as a basis to correlate the droplet lifetime in a convective environment (Meng et al., 2005) and with droplet interactions (Meng and Yang, 2007). We first focus on situations in which the droplet can instantaneously reach the supercritical regime (i.e., the pressure and temperature are above the dashed lines in Figure 11). The droplet surface is defined herein as the isotherm of the critical mixing temperature.

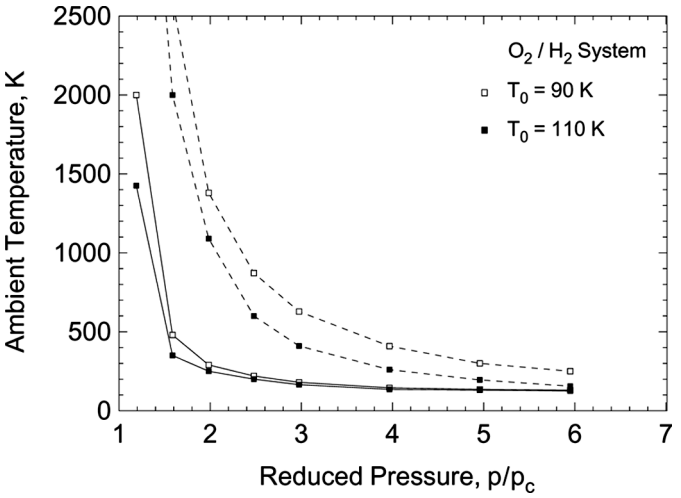

Figure 11 Limiting conditions for supercritical vaporization regime at two different initial droplet temperatures, $T_0 = 90$ and 110 K.

To facilitate data correlation, a simplified theoretical model is developed to provide an analytical basis. The thermal conductivity, specific heat, and thermal diffusion coefficient are taken as constants. In addition, the Stefan flow induced by droplet vaporization is assumed to be negligible. The problem is thus reduced to the following partial differential equation for the temperature field.

$$\frac{\partial T}{\partial t} = \alpha \frac{1}{r^2} \frac{\partial}{\partial r} \left(r^2 \frac{\partial T}{\partial r} \right) \tag{21}$$

Equation (21) can be normalized using the dimensionless quantities: $r^* = r/R_0, t^* = t\alpha/R_0^2$, and $T^* = (T_\infty - T)/(T_\infty - T_0)$. Equation (21) then becomes

$$\frac{\partial T^*}{\partial t^*} = \frac{1}{r^{*2}} \frac{\partial}{\partial r^*} \left(r^{*2} \frac{\partial T^*}{\partial r^*} \right) \tag{22}$$

subject to the initial conditions:

$$\begin{cases} T^*(r^*, 0) = 1, & \text{for } r^* \leq 1 \\ T^*(r^*, 0) = 0, & \text{for } r^* > 1 \end{cases} \tag{23}$$

The solution to Eq. (22) can be easily derived as (Rosner, 1967)

$$T^*(r^*, t^*) = \frac{1}{2} \left[\operatorname{erf}\left(\frac{1 + r^*}{\sqrt{4t^*}} \right) + \operatorname{erf}\left(\frac{1 - r^*}{\sqrt{4t^*}} \right) \right] - \frac{\sqrt{t^*}}{\sqrt{\pi} r^*} \left\{ \exp\left[\left(\frac{1 - r^*}{\sqrt{4t^*}} \right)^2 \right] - \exp\left[\left(\frac{1 + r^*}{\sqrt{4t^*}} \right)^2 \right] \right\} \tag{24}$$

The normalized droplet lifetime τ^* becomes only a function of the reduced critical temperature, $T_c^* = (T_\infty - T_c)/(T_\infty - T_0)$, and can be obtained by solving the following function:

$$T_c^* = \mathrm{erf}\left(\frac{1}{\sqrt{4\tau^*}}\right) - \frac{1}{\sqrt{\pi\tau^*}}\exp\left(-\frac{1}{4\tau^*}\right) \tag{25}$$

An extensive series of calculations have been conducted for two different initial droplet temperatures, $T_0 = 90$ and 110 K. The ambient temperature and pressure vary in the ranges of $500 \leq T_\infty \leq 2500$ K and $p_c \leq p \leq 300$ atm, respectively. It should be noted that, in some of the cases, the droplet may not be able to reach the supercritical regime instantaneously. The assumption of supercritical droplet vaporization in the preceding simple analysis thus cannot be satisfied.

Since the thermal diffusion and ensuing heat-up in the liquid phase is the limiting process during droplet vaporization, the dimensionless droplet lifetime is defined as

$$\tau^* = \tau\alpha_0^l/R_0^2 \tag{26}$$

where α_0^l denotes the liquid thermal diffusion coefficient at the initial state Figure 12 presents droplet lifetimes from both numerical calculations and theoretical analysis, Eq. (25). The filled dots correspond to the cases that do not satisfy the condition for instantaneously reaching the critical mixing state, i.e., the ambient pressure and temperature located underneath the dashed lines in Figure 11.

The difference between the numerical and theoretical results can be attributed to the simplifications in the approximate analysis. Since the droplet vaporization rate under supercritical conditions is dictated by the heat transfer at the droplet surface,

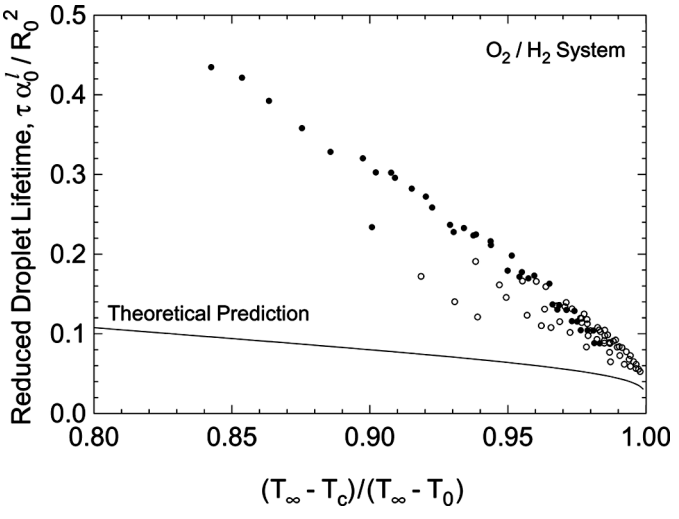

Figure 12 Variation of normalized droplet lifetime with a dimensionless parameter $(T_\infty - T_c)/(T_\infty - T_0)$.

both the thermal conductivity and temperature gradient at that location must be carefully evaluated. Figure 6 indicates that the thermal diffusivity, and conductivity as well, at the droplet surface remains almost fixed at the value in the liquid phase. The interface temperature gradient, however, varies with time, and can be approximately estimated as follows:

$$\nabla T|_s \approx \frac{T_\infty - T_c}{\sqrt{\alpha_\infty t}} \tag{27}$$

As the thermal diffusivity of the ambient gas increases, the interface temperature gradient decreases, leading to a longer droplet lifetime compared to cases with constant thermal diffusivity. It is then logical to improve the result in Figure 12 by introducing a correction factor in terms of the ratio α_∞/α_0^l. A detailed analysis of the numerical data suggests that the function below be employed to correlate the droplet lifetimes.

$$f(\alpha_\infty/\alpha_0^l) = 1 + 3.9\left[1 - \exp(-0.035(\alpha_\infty/\alpha_0^l - 1))\right] \tag{28}$$

A normalized droplet lifetime can now be defined as

$$\tau^*_{corrected} = \tau\alpha_0^l/[R_0^2 f(\alpha_\infty/\alpha_0^l)] \tag{29}$$

Figure 13 shows that droplet lifetimes under various conditions fall into a fairly straight line, and consequently can be correlated by a linear function in the following form:

$$\tau = \left[0.0115 + 0.542(1 - T_c^*)\right]\frac{R_0^2}{\alpha_0^l} f(\alpha_\infty/\alpha_0^l) \tag{30}$$

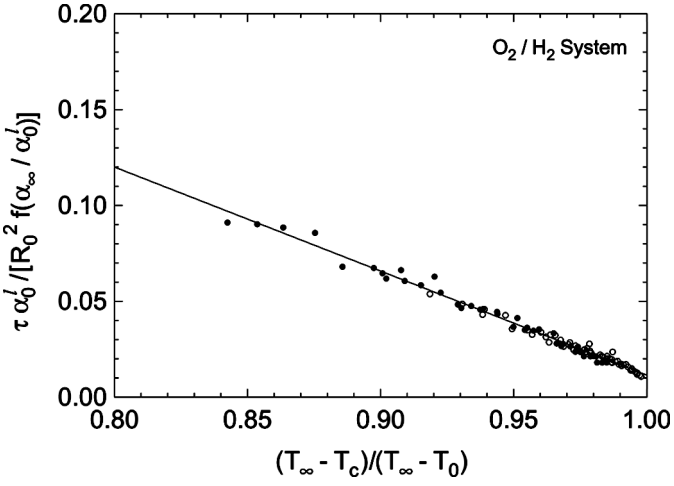

Figure 13 Variation of corrected droplet lifetime with a dimensionless parameter $(T_\infty - T_c)/(T_\infty - T_0)$.

The average and maximum estimation errors from this correlation are around 5% and 10%, respectively. Not surprisingly, this correlation has an excellent fit for droplet lifetimes in the supercritical regime, but it can also be extended to other cases (represented by filled dots in Figures 12 and 13) with good agreement. It should be mentioned that the reduced critical temperature T_c^* can be related to the Spalding number in the following form:

$$B_T = \frac{T_\infty - T_c}{T_c - T_0} = \frac{T_c^*}{1 - T_c^*} \tag{31}$$

Equation (30) clearly indicates that pressure affects droplet lifetime mainly through its effects on the critical mixing temperature and ambient thermal diffusion coefficient.

Droplet Vaporization in Hydrogen and Water Environments

In a practical rocket engine combustion chamber, the ambient environment surrounding the LOX droplet is not composed entirely of pure hydrogen. The effects of water vapor, produced through the combustion of oxygen and hydrogen, and its condensation near the droplet surface, need to be investigated. This section deals with LOX droplet vaporization in a gaseous mixture of hydrogen and water vapor under both subcritical and supercritical conditions. The droplet surface is chosen to be the isotherm of the critical mixing temperature.

The phenomenon of water condensation near the droplet surface is taken into account in the present study using the condensation model described before Figure 14 shows the distributions of the species concentrations at various times for $p = 100$ atm and $T_8 = 1000$ K. The ambient environment contains 50% water vapor. The accumulation of condensed water in the neighborhood of the droplet surface appears

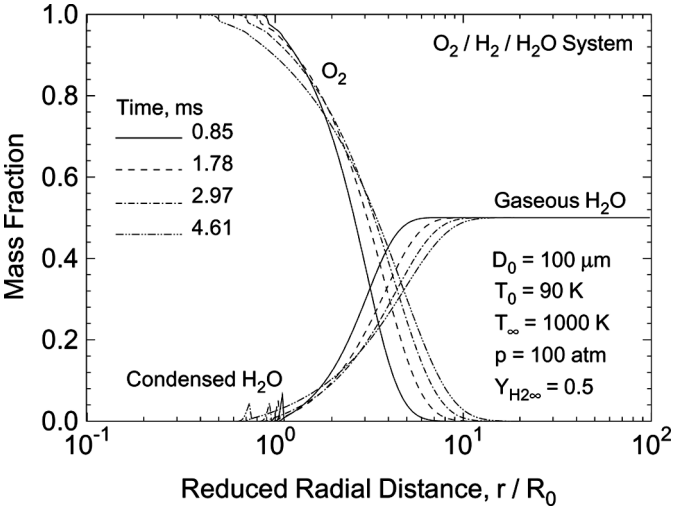

Figure 14 Distributions of species concentrations at various times, $LOX/H_2/H_2O$ system.

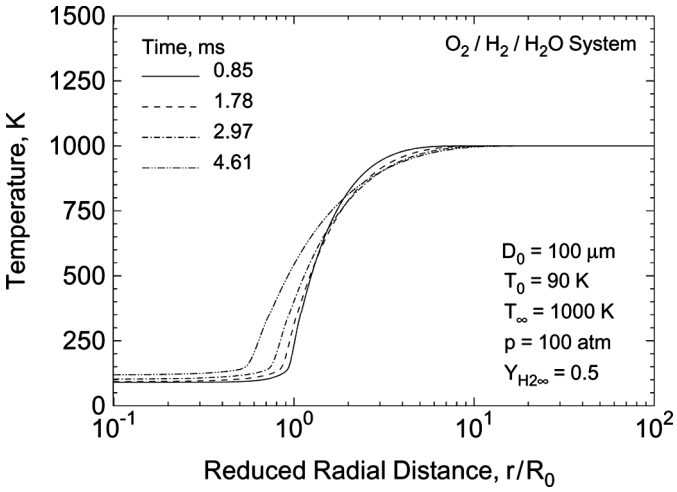

Figure 15 Temperature distributions at various times, $LOX/H_2/H_2O$ system.

to be very limited throughout the entire droplet lifetime, and eventually decreases to zero when the droplet disappears. The condensed liquid water particles, after their formation, are blown away from the droplet surface by the gaseous flow induced by droplet vaporization. As a result, only oxygen and hydrogen are present at the droplet surface. Water vapor does not reach the droplet surface. Figure 15 shows the corresponding temperature distributions. Although water condensation releases energy in the gaseous phase, no significant variation is observed on the temperature profiles. This further indicates that the amount of condensed liquid water present in the system remains very small during the droplet vaporization process.

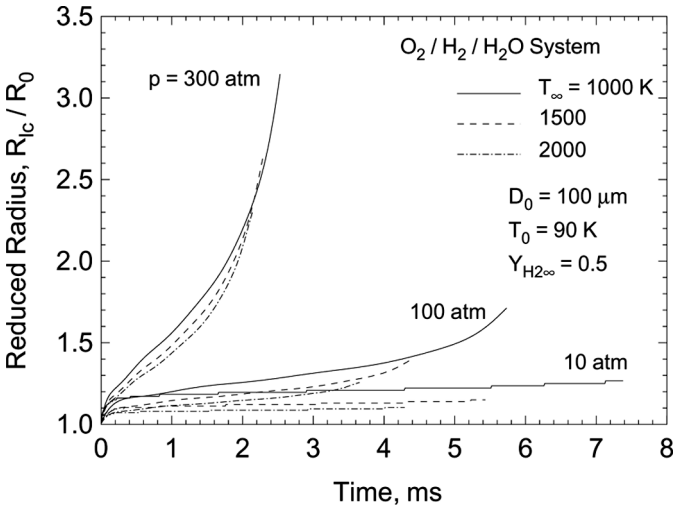

Figure 16 Transient variation of the condensation location closest to the droplet surface for different ambient temperatures and pressures.

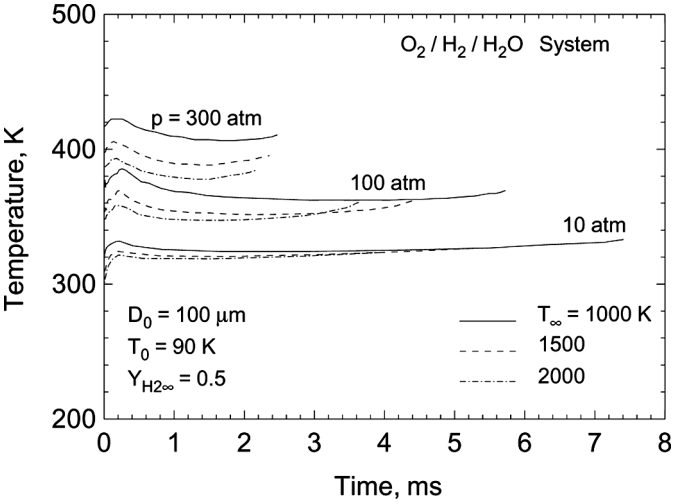

Figure 17 Transient variation of the temperature at the limiting condensation location for different ambient pressures and temperatures.

Figure 16 presents the transient variations of the condensation locations closest to droplet surface for the ambient pressure of 10–300 atm at 3 different temperatures of 1000, 1500, and 2000 K. The hydrogen mass fraction is initially 50%. As can be seen, condensation initially occurs very close to the oxygen droplet surface. The location then gradually moves away. Ambient pressure exerts a significant influence on the condensation location through its effect on the partial pressure of the water vapor. With increasing ambient pressure, the partial pressure of water vapor increases, implying that the condensation occurs in a higher temperature region

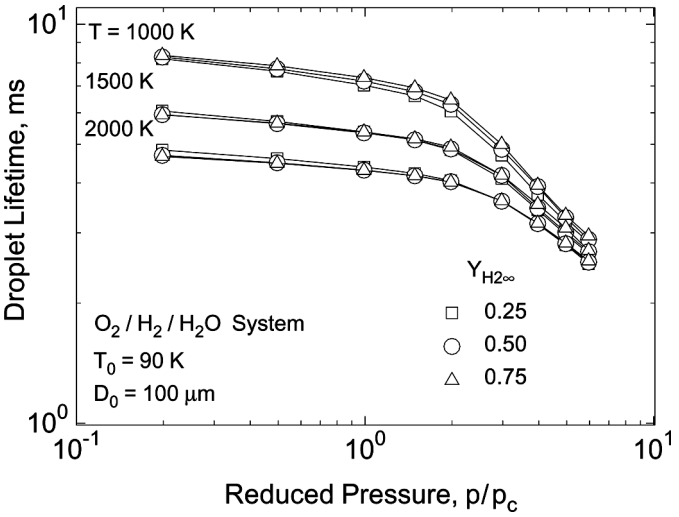

Figure 18 Variation of droplet lifetime with ambient pressure for various conditions.

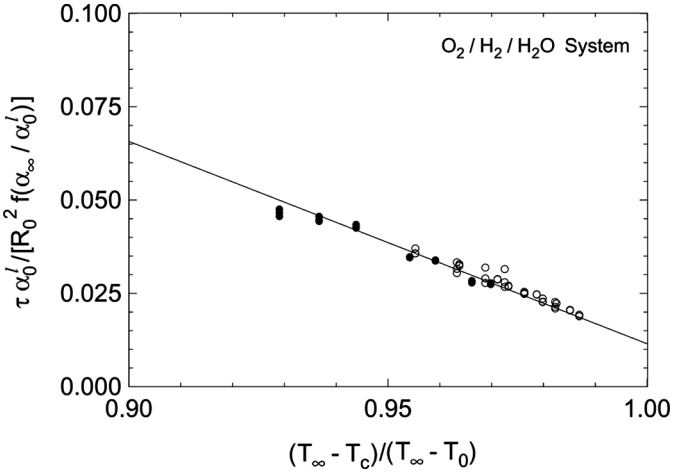

Figure 19 Corrected droplet lifetime as a function of dimensionless parameter $(T_\infty - T_c)/(T_\infty - T_0)$.

away from the droplet surface. The effect of the ambient temperature on the condensation location follows the same trend. This phenomenon is clearly depicted in Figure 17, which shows the temperature at the limiting condensation location.

In the present study, only water condensation is considered. The formation of ice particles is not treated, although this phenomenon would increase the amount of energy released during the phase change. Since the overall effects of water condensation on droplet vaporization are very small, the icing process is not expected to significantly change the results. In addition, a parametric study is conducted to determine the sensitivity of LOX droplet vaporization to the initial size of condensed water droplets by varying the value estimated by Eq. (10) by a factor of 10. No discernible changes are observed in terms of the LOX droplet lifetime and distributions of temperature and species concentrations.

Figure 18 presents droplet lifetimes over a broad range of the ambient temperatures of 1000–2000 K, pressures of 10–300 atm, and water mass fractions of 0.25–0.75. The effect of ambient composition on droplet lifetimes appears to be very weak. This conclusion is confirmed in Figure 19, in which the correlation obtained for pure hydrogen environments, Eq. (30), is found to have an excellent fit to the present data for mixed hydrogen and water environments, as well. The average and maximum deviations in this case are 4.8% and 12%, respectively.

CONCLUSIONS

Liquid oxygen (LOX) droplet vaporization in quiescent hydrogen and water environments were studied numerically over a wide range of ambient conditions. Both sub- and super-critical pressures were considered. The model was based on complete conservation equations in a spherically symmetric coordinate, and incorporated a unified treatment of general fluid thermodynamics and transport phenomena valid for the entire regime of fluid thermodynamic states. In addition, a water-vapor

condensation model was included for treating the phase change near the droplet surface. Various underlying mechanisms dictating the characteristics of high-pressure droplet vaporization were identified. The effects of the Dufour and Soret cross-diffusion terms were also examined and found to exert negligible influences in determining the droplet behavior. Finally, correlations for droplet lifetimes were established for both LOX/hydrogen and LOX/hydrogen/water systems in terms of initial droplet properties and ambient conditions. The result can be used as a basis for further estimating droplet lifetimes in convective hydrogen streams and with droplet interactions.

NOMENCLATURE

A	surface area
B	Spalding number
C_p	constant-pressure specific heat
D	droplet diameter
D_{ij}	binary mass diffusion coefficient
D_{im}	effective mass diffusion coefficient
D_{Ti}	thermal diffusion coefficient
e	specific total internal energy
F_T	thermophoretic force
F_v	viscous force
$\bar{h}_I$	partial mass enthalpy of species i
J	homogeneous nucleation rate
Kn	Knudson number
K_{vap}	vaporization kinetic coefficient
$\dot{m}$	droplet mass evaporation rate
N	number of species
p	pressure
q_e	energy diffusion flux
q_i	mass diffusion flux of species i
r	radial coordinate
R	droplet radius
R_u	Universal gas constant
S	saturation ratio
T	temperature
v	velocity
w	control surface moving velocity
V	total volume
V_i	diffusion velocity of species i
X_i	mole fraction of species i
Y_i	mass fraction of species i
W	molecular weight

Greek Symbols

α	thermal diffusion coefficient
λ	thermal conductivity or molecular mean free path
μ	viscosity
μ_i	chemical potential of species i
ρ	density
σ	surface tension
τ	droplet lifetime
ω	chemical reaction rate

Subscripts

0	initial condition
c	critical condition
i	species *i*
p	condensed particle
r	reduced thermodynamic property
sat	saturation value
∞	ambient condition

Superscripts

g	gaseous phase
l	liquid phase
0	ideal gas limit
$\bullet$	time derivative
$*$	dimensionless quantity

REFERENCES

Bellan, J. (2000) Supercritical (and subcritical) fluid behavior and modeling: Drops, streams, shear and mixing layers, jets, and spray. *Prog. Energy Combust. Sci.*, **26**, 221–295.

Brock, J.R. (1962) On the theory of thermal forces acting on aerosol particles. *J. Colloid Sci.*, **17**, 768–780.

Callen, H.B. (1985) *Thermodynamics and an Introduction to Thermostatistics*, 2nd ed., John Wiley & Sons, New York.

Carlson, D.J. and Haglund, R.F. (1964) Particle drag and heat transfer in rocket nozzles. *AIAA J.*, **2**, 35–58.

Curtis, E.W. and Farrel, P.V. (1992) A numerical study of high pressure vaporization. *Combust. Flame*, **90**, 85–102.

Daou, J., Haldenwang, P., and Nicoli, C. (1995) Supercritical burning of liquid (LOX) droplet with detailed chemistry. *Combust. Flame*, **101**, 153–169.

Daou, J. and Rogg, B. (1998) Convective burning of gaseous fuel pockets and supercritical droplets. *Combust. Flame*, **115**, 145–157.

Delplanque, J.P. and Sirignano, W.A. (1993) Numerical study of the transient vaporization of an oxygen droplet at sub- and super-critical conditions. *Intl. J. Heat Mass Transfer*, **36**, 303–314.

Ely, J.F. and Hanley, H.J. (1981) Prediction of transport properties. 1. Viscosity of fluids and mixtures. *Ind. Eng. Chem. Fundamentals*, **20**, 323–332.

Ely, J.F. and Hanley, H.J. (1983) Prediction of transport properties. 2. thermal conductivity of pure fluids and mixtures. *Ind. Eng. Chem. Fundamentals*, **22**, 90–97.

Harstad, K. and Bellan, J. (1998a) Isolated fluid oxygen drop behavior in fluid hydrogen at rocket chamber pressures. *Intl. J. Heat Mass Transfer*, **41**, 3537–3550.

Harstad, K. and Bellan, J. (1998b) Interactions of fluid oxygen drops in fluid hydrogen at rocket chamber pressures. *Intl. J. Heat Mass Transfer*, **41**, 3551–3558.

Hsiang, L.P. and Faeth, G.M. (1992) Near-limit drop deformation and secondary breakup. *Intl. J. Multiphase Fl.*, **18**, 635–652.

Hsieh, K.C., Shuen, J.S., and Yang, V. (1991) Droplet vaporization in high-pressure environments I: Near critical conditions. *Combust. Sci. Technol.*, **76**, 111–132.

Jia, H. and Gogos, G. (1993) High pressure droplet vaporization; Effects of liquid-phase gas solubility. *Intl. J. Heat Mass Transf.*, **36**, 4419–4431.

Jiang, T.L. and Chiang, W.T. (1994) Effects of multiple droplet interaction on droplet vaporization in subcritical and supercritical pressure environments. *Combust. Flame*, **97**, 17–34.

Jiang, T.L. and Chiang, W.T. (1996) Transient heating and vaporization of a cool dense cloud of droplets in hot supercritical surroundings. *Intl. J. Heat Mass Transfer*, **39**, 1023–1031.

Lafon, P. (1995) *Modélisation et Simulation Numérique de L'Evaporation et de la Combustion de Gouttes à Haute Pression*, Ph.D Thesis, à l'Université d'Orléans, France.

Litchford, R.J. and Jeng, S.-M. (1990) LOX vaporization in high-pressure, hydrogen-rich gas. AIAA Paper 90–2191, *AIAA Twenty-Sixth Joint Propulsion*, Conference, Orlando, FL.

McDonald, J.E. (1962) Homogeneous nucleation of vapor condensation. 1. Thermodynamic aspects. *Amer. J. Phys.*, **30**, 870–877.

Meng, H., Hsiao, G.C., Yang, V., and Shuen, J.S. (2005) Transport and dynamics of liquid oxygen droplets in supercritical hydrogen streams. *J. Fluid Mech.*, **527**, 115–139.

Meng, H. and Yang, V. (1998) Interactions of liquid oxygen vaporization in high pressure hydrogen environment. AIAA Paper 98–3537, *34th AIAA/ASME/SAE/ASEE Joint Propulsion Conference & Exhibit*, July 13–15, Cleveland, OH.

Meng, H. and Yang, V. (2003) A unified treatment of general fluid thermodynamics and its application to a preconditioning scheme. *J. Comput. Phys.*, **189**, 277–304.

Meng, H. and Yang, V. (2007) Transport and dynamics of two liquid oxygen (LOX) droplets in tandem in supercritical hydrogen streams, to be submitted to *Combust. Sci. Technology*.

Powell, E.E. (1988) Simulation of water vapor condensation on LOX droplet surface using liquid nitrogen. *NASA/ASEE Summer Faculty Fellowship Program*, NGT 01-002-099, N89-21726 14-99.

Reid, R.C., Prausnitz, J.M., and Poling, E.P. (1987) *The Properties of Gases and Liquids*, 4th ed., McGraw Hill, New York.

Reist, P.C. (1984) *Introduction to Aerosol Science*, MacMillan Publishing Company, New York.

Rogers, R.R. and Yau, M.K. (1989) *A Short Course in Cloud Physics*, 3rd ed., Pergamon Press.

Rosner, D.E. (1967) On liquid droplet combustion at high pressures. *AIAA J.*, **5**, 163–166.

Shuen, J.S., Yang, V., and Hsiao, C.C. (1992) Combustion of liquid-fuel droplet in supercritical conditions. *Combust. Flame*, **89**, 299–319.

Sirignano, W.A. and Delplanque J.P. (1999) Transcritical vaporization of liquid fuels and propellants. *J. Prop. Power*, **15**, 896–902.

Talbot, L., Cheng, R.K., Schefer, R.W., and Willis, D.R. (1980) Thermophoresis of particles in a heated boundary layer. *J. Fluid Mech.*, **101**, 737–758.

Takahashi, S. (1974) Preparation of a generalized chart for the diffusion coefficients of gases at high pressures. *J. Chem. Eng. (Japan)*, **7**, 417–420.

Yang, V. (2001) Modeling of Supercritical Vaporization, Mixing, and Combustion Processes in Liquid-Fueled Propulsion Systems, *Proc. Combust. Instit.*, **28**, 925–942.

Yang, V., Lin, N.N., and Shuen, J.S. (1994) Vaporization of liquid oxygen (LOX) droplets in supercritical hydrogen environments. *Combust. Sci. Technol.*, **97**, 247–270.

Zong, N., Meng, H., Hiesh, S.-Y., and Yang, V. (2004) A numerical study of cryogenic fluid injection and mixing under supercritical conditions. *Phys. Fluids*, **16**, 4248–4261.

Zong, N. and Yang, V. (2006) Cryogenic fluid jets and mixing layers in transcritical and supercritical environments. *Combust. Sci. Technol.*, **178**, 193–227.

Zong, N. and Yang, V. (2007) Near-field flow and flame dynamics of LOX/Methane shear coaxial injector under supercritical conditions, *Proc. Combust. Instit.*, **31**, 2309–2317.